Size-Induced Ferroelectricity in Antiferroelectric Oxide Membranes

Ruijuan Xu, Kevin J Crust, Varun Harbola, Rémi Arras, Kinnary Y Patel, Sergey Prosandeev, Hui Cao, Yu-tsun Shao, Piush Behera, Lucas Caretta, et al.

To cite this version:

Ruijuan Xu, Kevin J Crust, Varun Harbola, Rémi Arras, Kinnary Y Patel, et al.. Size-Induced Ferroelectricity in Antiferroelectric Oxide Membranes. Advanced Materials, 2023, 35 (17), pp.2210562. 10.1002/adma.202210562 . hal-04237736

HAL Id: hal-04237736
https://hal.science/hal-04237736
Submitted on 11 Oct 2023

Size-Induced Ferroelectricity in Antiferroelectric Oxide Membranes

Ruijuan Xu, Kevin J. Crust, Varun Harbola, Rémi Arras, Kinnary Y. Patel, Sergey Prosandeev, Hui Cao, Yu-Tsun Shao, Piush Behera, Lucas Caretta, Woo Jin Kim, Aarushi Khandelwal, Megha Acharya, Melody M. Wang, Yin Liu, Edward S. Barnard, Archana Raja, Lane W. Martin, X. Wendy Gu, Hua Zhou, Ramamoorthy Ramesh, David A. Muller, Laurent Bellaiche, and Harold Y. Hwang*

Despite extensive studies on size effects in ferroelectrics, how structures and properties evolve in antiferroelectrics with reduced dimensions still remains elusive. Given the enormous potential of utilizing antiferroelectrics for high-energy-density storage applications, understanding their size effects will provide key information for optimizing device performances at small scales. Here, the fundamental intrinsic size dependence of antiferroelectricity in lead-free $NaNbO_3$ membranes is investigated. Via a wide range of experimental and theoretical approaches, an intriguing antiferroelectric-to-ferroelectric transition upon reducing membrane thickness is probed. This size effect leads to a ferroelectric single-phase below 40 nm, as well as a mixed-phase state with ferroelectric and antiferroelectric orders coexisting above this critical thickness. Furthermore, it is shown that the antiferroelectric and ferroelectric orders are electrically switchable. First-principle calculations further reveal that the observed transition is driven by the structural distortion arising from the membrane surface. This work provides direct experimental evidence for intrinsic size-driven scaling in antiferroelectrics and demonstrates enormous potential of utilizing size effects to drive emergent properties in environmentally benign lead-free oxides with the membrane platform.

1. Introduction

Size effects, which study the change in properties with decreasing physical dimensions, have received considerable attention due to increasing demand for enhanced functionalities in miniaturized electronics. Extensive studies about size effects have been performed in functional materials such as ferroelectrics for over five decades.[1–4] It is generally accepted that ferroelectricity persists above a certain critical thickness that relates to an intrinsic limit,[5] the electrical and mechanical boundary conditions,[6–9] as well as extrinsic factors related to processing.[10] Recent work has also shown a giant polarization in freestanding $BiFeO_3$ films when approaching the 2D limit.[11]

As an important energy storage material, antiferroelectrics hold great promise for high-energy density capacitors, high-strain actuators, and electrocaloric

---

R. Xu, W. J. Kim, A. Khandelwal, H. Y. Hwang
Department of Applied Physics
Stanford University
Stanford, CA 94305, USA

R. Xu, K. J. Crust, V. Harbola, W. J. Kim, A. Khandelwal, H. Y. Hwang
Stanford Institute for Materials and Energy Sciences
SLAC National Accelerator Laboratory
Menlo Park, CA 94025, USA

R. Xu, Y. Liu
Department of Materials Science and Engineering
North Carolina State University
Raleigh, NC 27606, USA
E-mail: rxu22@ncsu.edu

The ORCID identification number(s) for the author(s) of this article can be found under https://doi.org/10.1002/adma.202210562.

DOI: 10.1002/adma.202210562

K. J. Crust, V. Harbola
Department of Physics
Stanford University
Stanford, CA 94305, USA

R. Arras
CEMES
Université de Toulouse
CNRS
UPS, 29 rue Jeanne Marvig F-31055, Toulouse, France

K. Y. Patel, S. Prosandeev, L. Bellaiche
Physics Department and Institute for Nanoscience and Engineering
University of Arkansas
Fayetteville, AR 72701, USA

H. Cao
Materials Science Division
Argonne National Laboratory
Lemont, IL 60439, USA

Y.-T. Shao, D. A. Muller
Department of Applied and Engineering Physics
Cornell University
Ithaca, NY 14853, USA

cooling.[12,13] As compared to ferroelectrics, however, considerably less work pertaining to size effects has been performed in antiferroelectrics. First-principle calculations predict an intrinsic size-driven scaling behavior in antiferroelectric materials, with a critical thickness below which an antiferroelectric-to-ferroelectric transition occurs due to the intrinsic surface contribution.[14] This size effect, however, has not been verified experimentally. This is primarily due to the challenge to completely decouple the effects of strain, which becomes predominant in thin films in the ultrathin limit. Thus, the strain-induced antiferroelectric-to-ferroelectric transition overrides the intrinsic size-driven transition, making it difficult to probe intrinsic scaling. Completely decoupling the strain effects in antiferroelectric thin-film heterostructures, however, is not trivial due to the lattice mismatch between antiferroelectric films and commercially available substrates, thus limiting the direct experimental probe of the intrinsic size effects in antiferroelectrics.

The ability to create crystalline oxide membranes enables new opportunities to probe the intrinsic size effects in antiferroelectrics.[11,15–20] By releasing epitaxial films from substrates, strain exerted by the substrate can be minimized in oxide membranes. Therefore, by varying the membrane thickness, the intrinsic size-driven scaling behavior can be directly probed. Here, we focus on $NaNbO_3$ which is known as a promising lead-free alternative to replace lead-based antiferroelectrics and as one of the most complex perovskites exhibiting a rich spectrum of ground states and temperature-dependent phase transition.[21,22] So far, the majority of experimental work on $NaNbO_3$ has been focused on its bulk antiferroelectric phase at room temperature. It is possible to tweak the phase stability from an antiferroelectric to a ferroelectric phase in bulk $NaNbO_3$ with temperature,[23,24] chemical substitution,[25] electric field,[26] and particle size.[27,28] In addition, recent work has also demonstrated epitaxial growth of $NaNbO_3$ films on single crystalline substrates.[29,30]

Here, in order to probe the intrinsic size effects in antiferroelectric films, we synthesized high crystalline quality $NaNbO_3$ freestanding membranes with varying thickness using thin-film epitaxy and epitaxial lift-off techniques. Utilizing scanning probe microscopy and optical measurements, we probe an intriguing size-driven antiferroelectric-to-ferroelectric phase transition upon reducing thickness, with the presence of a ferroelectric phase for thicknesses below 40 nm and the coexistence of ferroelectric and antiferroelectric phases above 40 nm. Furthermore, we note that the antiferroelectric and ferroelectric phases are electrically switchable. This emergent phase transition also impacts the nanomechanical properties of the $NaNbO_3$ membranes, giving rise to a non-monotonic thickness dependence of the Young's modulus.

2. Results and Discussion

2.1. Synthesis of $NaNbO_3$ Membranes and Thickness-Dependent Structural Evolution

Epitaxial heterostructures of $NaNbO_3$ thin films with thickness (t) ranging from 9 to 164 nm were prepared on single-crystalline $SrTiO_3$ (001) substrates with a 20 nm $La_{0.7}Sr_{0.3}MnO_3$ sacrificial buffer layer synthesized via pulsed laser deposition (PLD). We dissolved $La_{0.7}Sr_{0.3}MnO_3$ in a hydrochloric acid (HCl) and potassium iodide (KI) mixed solution to release $NaNbO_3$ films from the substrate and transferred these freestanding membranes onto 200 nm-thick SiN_x membranes with arrays of holes in a diameter of 2–10 μm, creating circular drumheads (Experimental Section; **Figure 1**a,b and Figure S1, Supporting Information). To examine the crystalline quality of the lifted-off $NaNbO_3$ membranes, we performed high-angle annular dark-field scanning transmission electron microscopy (STEM) imaging on these plan-view samples. The atomic-scale STEM images obtained for the 13 and 65 nm-thick membranes reveal high crystalline quality (Figure 1c,d and Figure S2, Supporting Information). We carried out θ–2θ X-ray diffraction (XRD) studies about the $NaNbO_3$ 002-diffraction condition to characterize the structure and strain conditions of these membranes. For $t < 40$ nm, these films remain as a single phase, whereas for $t \geq 40$ nm, another peak emerges at a higher 2θ angle indicating the presence of another structural phase (Figure 1e). In contrast, the as-grown films on $SrTiO_3$ substrates remain as a single phase throughout the entire

---

Y.-T. Shao
Mork Family Department of Chemical Engineering and Materials Science
University of Southern California
Los Angeles, CA 90089, USA

P. Behera, L. Caretta, M. Acharya, L. W. Martin
Department of Materials Science and Engineering
University of California
Berkeley, Berkeley, CA 94720, USA

L. Caretta
School of Engineering
Brown University
Providence, RI 02912, USA

M. Acharya, L. W. Martin
Materials Sciences Division
Lawrence Berkeley National Laboratory
Berkeley, CA 94720, USA

M. M. Wang
Department of Materials Science and Engineering
Stanford University
Stanford, CA 94305, USA

E. S. Barnard, A. Raja
The Molecular Foundry
Lawrence Berkeley National Laboratory
1 Cyclotron Road, Berkeley, CA 94720, USA

X. W. Gu
Department of Mechanical Engineering
Stanford University
Stanford, CA 94305, USA

H. Zhou
X-ray Science Division
Advanced Photon Source
Argonne National Laboratory
Lemont, IL 60439, USA

R. Ramesh
Department of Materials Science and Nanoengineering
Department of Physics and Astronomy
Rice University
Houston, TX 77251, USA

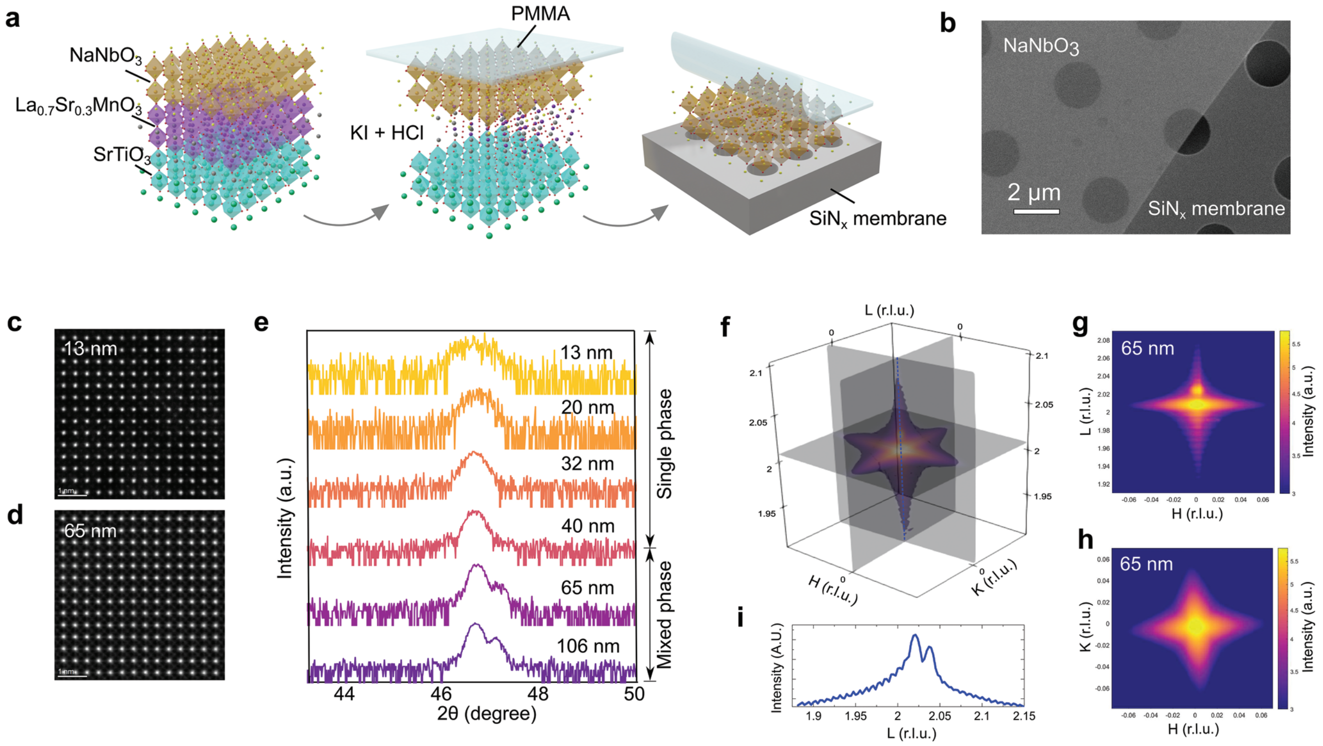

Figure 1. Structural characterization of freestanding NaNbO$_3$ membranes. a) Schematics illustrating the lift-off process for NaNbO$_3$ membranes. By dissolving La$_{0.7}$Sr$_{0.3}$MnO$_3$ in a mixed KI and HCl solution, NaNbO$_3$ are released and transferred onto 200 nm-thick SiN$_x$ membranes with arrays of holes in a diameter of 2–10 µm. b) Scanning electron microscopy images showing the NaNbO$_3$ laminated on the holes of SiN$_x$ membranes to create freestanding circular drumheads. c,d) High-angle annular dark-field scanning transmission electron microscopy images obtained for the 13 nm (c) and 65 nm (d) NaNbO$_3$ membranes, revealing high crystalline quality. e) θ–2θ X-ray diffraction about the NaNbO$_3$ 002-diffraction condition as a function of thickness showing a single-phase state for membranes below 40 nm and phase coexistence for membranes above 40 nm. f) Synchrotron-based 3D reciprocal space maps about the NaNbO$_3$ 002-diffraction condition for 65 nm membranes, showing a clear phase segregation with fundamentally different structural characteristics in these phases, g,h) illustrated in the slices of *H*–*L* (g) and *H*–*K* (h) reciprocal planes. The *H*–*K* map was sliced perpendicular to the *L* axis at *L* = 2.02. The map sliced from the *K*–*L* reciprocal plane is similar to the results from the *H*–*L* plane, which is not shown here. i) The 002-line scan cut along the *L* axis of the 3D RSM in (f).

thickness range, suggesting that the mixed-phase state only exists in membranes that are released from the substrates (Figure S3, Supporting Information). The out-of-plane lattice parameters extracted for these two phases show small variations with thickness, indicating these freestanding NaNbO$_3$ membranes have similar strain conditions regardless of film thickness (Figure S4, Supporting Information). We also performed 2D XRD reciprocal space maps (RSMs) as a function of thickness about the NaNbO$_3$ 103-diffraction condition, which reveal small variations in the in-plane lattice parameters of each phase, confirming that the NaNbO$_3$ membranes possess similar amount of strain (Figure S5, Supporting Information). Note that the lattice parameters extracted for these two phases are very different, indicating they indeed originate from different structural phases rather than different orientations of one structural phase. In order to explore more structural details for these two structural phases, we measured 3D RSMs about the NaNbO$_3$ 002-diffraction condition in 65 nm-thick membranes using synchrotron XRD (Figure 1f). First, the clear Laue oscillations present in the synchrotron XRD 002-line scan confirm the high crystalline quality of the membranes (Figure 1i). In addition, the obtained results reveal two phases segregating along the *L* axis with different *L* values in the *H*–*L* reciprocal plane, exhibiting fundamentally different structural characteristics (Figure 1f–h). In particular, the phase with the lower *L* value also shows four satellite peaks in the *H*–*K* reciprocal plane, reminiscent of the results generated by periodic domain structures in ferroelectrics.

2.2. Piezoresponse Force Microscopy Measurements Probing the Emergence of Ferroelectricity

Intrigued by these observations, we performed piezoresponse force microscopy (PFM) to explore the possible presence of polar order in the NaNbO$_3$ membranes. Since NaNbO$_3$ is antiferroelectric in bulk, we would expect similar properties to occur in these strain-free membranes. Instead of measuring weak PFM response, which is expected for antiferroelectric materials, we probed strong irregular lateral domain patterns for $t \leq$ 13 nm, indicating that the membranes possess in-plane polarized domains with no out-of-plane component at this thickness (**Figure** 2a,b and Figures S6 and S7, Supporting Information). With increasing thickness, the out-of-plane component emerges resulting in a stripe domain pattern with both lateral and vertical PFM response for thickness between 13 and 40 nm (Figure 2c,d

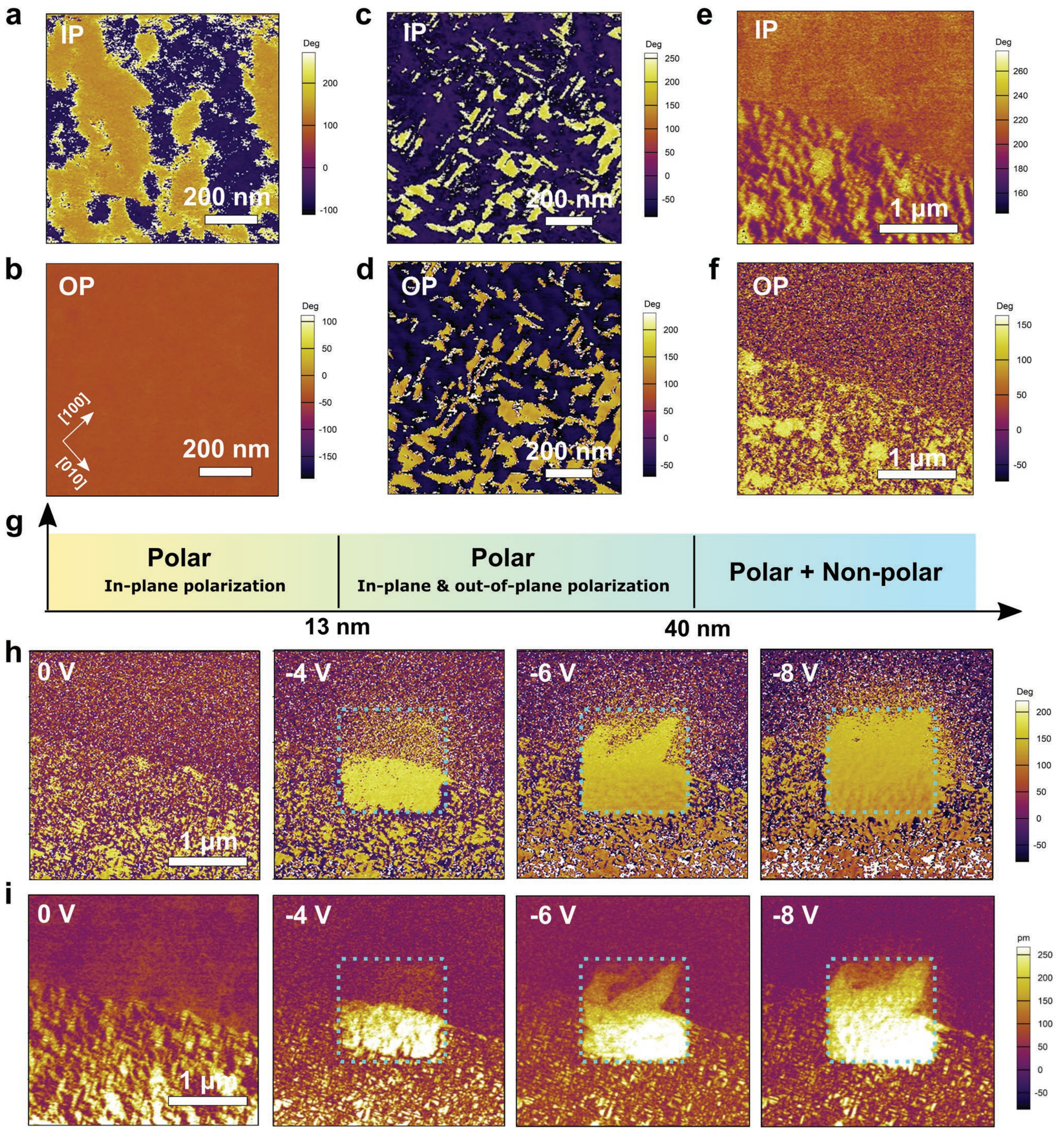

Figure 2. PFM images of emergent ferroelectricity and phase coexistence in $NaNbO_3$ membranes. a–f) Lateral and vertical PFM phase images obtained for 13 nm-thick (a,b), 40 nm-thick (c,d), and 100 nm-thick (e,f) membranes, respectively. g) Schematic phase diagram summarizing the observed ferroic orders in three thickness regimes of $NaNbO_3$ membranes probed by PFM. h,i) Vertical phase (h) and amplitude (i) PFM images measured near the mixed phase region in the 100 nm-thick membranes after applying a tip bias of 0, −4, −6, and −8 V.

and Figures S6 and S7, Supporting Information). This thickness-dependent domain structure evolution is likely a result of the depolarization effect. Since the out-of-plane depolarization field increases with decreasing film thickness, the membrane adopts pure in-plane polarization to minimize the increased out-of-plane depolarization field in thinner membranes when $t \leq 13$ nm. Moreover, for thickness above 40 nm we note that the stripe domains are also accompanied by some non-polar regions with diminished PFM response (Figure 2e,f and Figure S8, Supporting Information). These polar and non-polar phases coexist on the micrometer lateral scale, which is consistent with the observed phase coexistence from XRD. Such a thickness-dependent

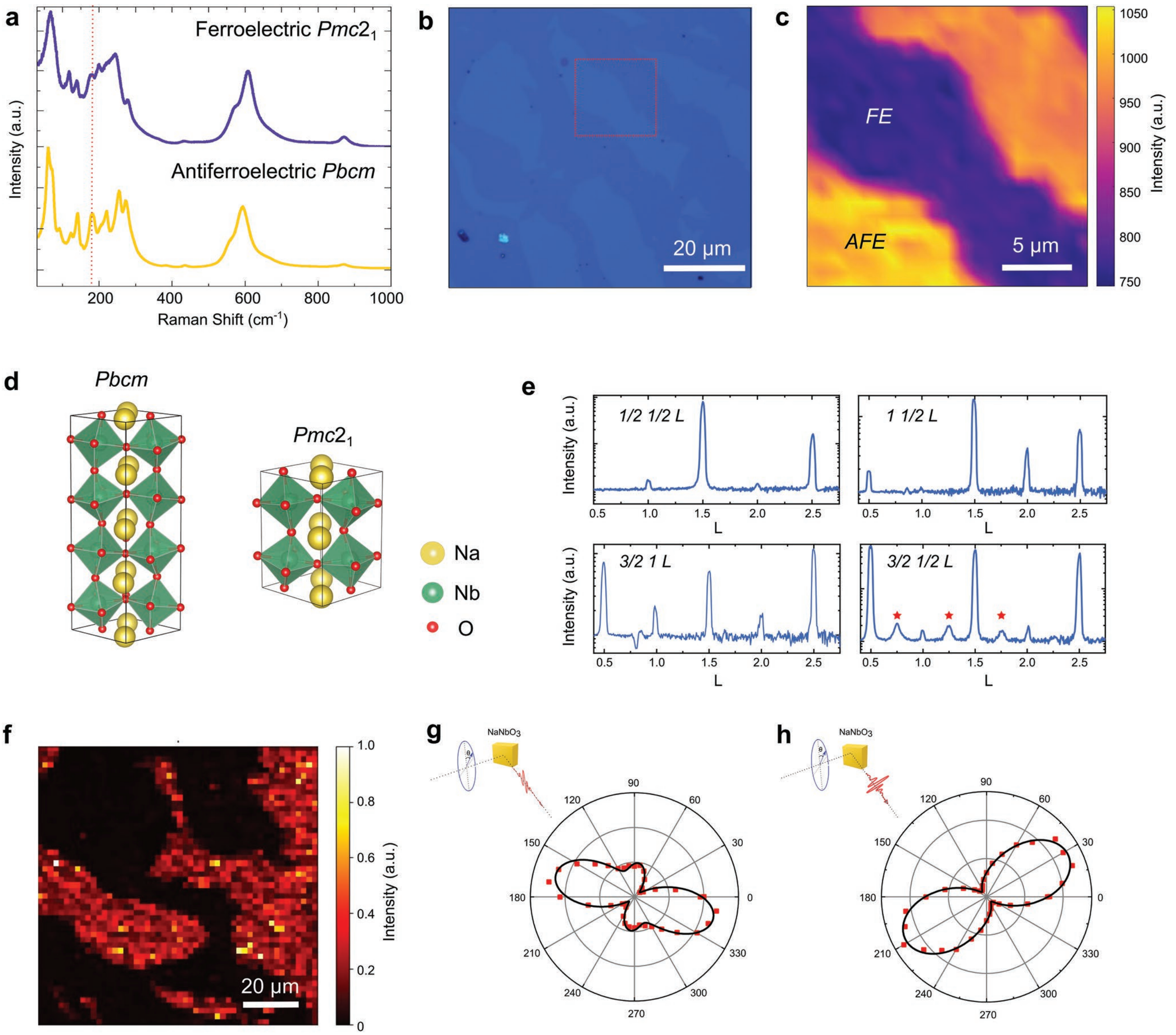

Figure 3. Probing space group symmetry of ferroelectric and antiferroelectric phases. a) Raman spectra obtained for both the ferroelectric and antiferroelectric phases in 164 nm-thick $NaNbO_3$, corresponding to $Pmc2_1$ and $Pbcm$ space groups, respectively. b) Optical images revealing the phase coexistence with distinct optical contrast. c) 2D Raman mapping by integrating the Raman intensity near 178 cm^{-1} showing a similar pattern as observed optically. d) Schematics illustrating the unit cells for $Pbcm$ and $Pmc2_1$ space groups. e) Representative X-ray half-order Bragg diffraction patterns for $NaNbO_3$ membranes. Note that a background powder ring peak appears in the ($\frac{3}{2}$ 1 L) scan near $L = 0.75$. Quarter-integer Bragg peaks arising from the quadruple lattice of the $Pbcm$ phase are marked by asterisks. f) 2D SHG mapping on the mixed phase region with bright intensity generated by the non-centrosymmetric ferroelectric phase and dark intensity generated by the centrosymmetric antiferroelectric phase. g,h) SHG polar plots measured from the ferroelectric phase as a function of incident beam polarization with the emitted signal either vertically (g) or horizontally (h) polarized.

structural evolution is summarized in Figure 2g, showing three thickness regimes with different domain structures. As to the thickness at which the polar phase completely vanishes, we cannot experimentally probe it at this time due to difficulties releasing very thick intact membranes. Instead, we extrapolated this thickness from the X-ray θ–2θ line scans by performing Gaussian fits to extract the relative intensities of the peaks for the two phases (Figure S9, Supporting Information). The extrapolated thickness is found to be 268 nm, above which the $NaNbO_3$ membrane will likely become completely non-polar.

We further performed local switching experiments to understand how these polar and non-polar phases respond to an external bias. By applying an electrical bias of −4 V to 106 nm-thick membranes, only the polar phases are electrically switched (Figure 2h,i and Figure S10, Supporting Information). The non-polar phase, although unswitchable at −4 V, can be switched into a polar phase partially at −6 V and completely at −8 V, and remains polar when the field is removed. Likewise, reversing the sign of the applied bias also shows similar switching behaviors but with a flipped domain contrast

(Figure S11, Supporting Information). These results indicate that these polar phases are ferroelectric, whereas the non-polar phase can also transform into a polar phase upon application of high electric field.

2.3. Optical Measurements Revealing Structural Nature of the Phase Transition

2.3.1. Raman Spectroscopy

In order to elucidate the structural nature of the polar and non-polar phases, we studied the space group symmetry of these phases using a combination of Raman spectroscopy, X-ray half-order diffraction, and second-harmonic generation (SHG) measurements. We began by obtaining Raman spectra of both the polar and non-polar phases of $NaNbO_3$ for a 164 nm-thick membrane across a wavenumber range of 30–1000 cm^{-1} (**Figure 3**a). Comparing the general spectral features with previous results for powder samples,[31–33] the space group symmetry of both phases can be identified, from which we obtain a non-centrosymmetric space group $Pmc2_1$ for the ferroelectric phase and a centrosymmetric space group $Pbcm$ for the non-polar phase (Figures S12 and S13 and Table S1, Supporting Information). Since $Pbcm$ is consistent with antipolar ordering, these results indicate that the observed non-polar phase is antiferroelectric in nature. Further measurements were performed on samples across the entire thickness range to ensure that the Raman peak locations for the ferroelectric phase remain relatively constant as a function of thickness (Figure S14, Supporting Information). Such a coexistence of ferroelectric and antiferroelectric phases can even be recognized optically through their distinct optical contrast (see Figure 3b for the result at $t = 164$ nm and Figure S15, Supporting Information, for results above 40 nm). To ensure that the optical contrast corresponds to these two phases, Raman spectral mapping was performed across a 20 µm × 20 µm region on a 164 nm-thick membrane transferred onto an Al_2O_3 substrate, which provides minimal Raman spectral background across the region of interest (100–300 cm^{-1}) and allows for a larger mapping area than can be achieved with the drumheads on SiN_x membranes (Figure 3c). By integrating the Raman intensity near 178 cm^{-1} at which the antiferroelectric phase shows a much higher peak intensity than the ferroelectric phase, we probed a similar pattern in the Raman mapping as observed by optical microscopy. These results indicate that the antiferroelectric and ferroelectric phases are distributed on the micrometer scale and remain homogeneous within each phase region.

2.3.2. Half-Order X-ray Diffraction Studies

We also performed synchrotron-based half-order XRD studies to further verify the structural characteristics of these two phases in terms of lattice periodicity and octahedral rotation. For instance, $Pmc2_1$ exhibits a rotation pattern of a^-a^-c+, leading to a $\sqrt{2}a_p \times \sqrt{2}a_p \times 2a_p$ supercell (a_p is the lattice parameter of cubic perovskite subcell), whereas $Pbcm$ exhibits a complicated rotation pattern of $a^-a^-c^+/a^-a^-c^-$ giving rise to a $\sqrt{2}a_p \times \sqrt{2}a_p \times 4a_p$ supercell (Figure 3d and Figure S16, Supporting Information). This distinct octahedral rotation pattern can be detected via half-order XRD. Given the structural complexity, we only discuss the octahedral rotation patterns qualitatively without quantifying the value of rotation angles. Here a series of half-integer Bragg peaks at $\left(\frac{h}{2}, \frac{k}{2}, \frac{l}{2}\right)$ were measured with h, k, and l being odd integers except those that satisfy $h = k = l$ which are forbidden. In addition, the half-integer Bragg peaks with one of the h, k, and l being an even integer were also measured (Figure 3e and Figure S17, Supporting Information). Following Glazer's extinction rules,[34] we can determine the following possible rotation patterns in the $NaNbO_3$ membranes: $a^+b^-c^-$, $a^-b^+c^-$, and $a^-b^-c^+$. These results are consistent with the rotation pattern generated by the $Pmc2_1$ structural domains with the long axis of the supercell lying either in-plane or out-of-plane (see Note S1 and Table S2, Supporting Information). Moreover, we measured a set of quarter-integer Bragg peaks at $\left(\frac{3}{2}, \frac{1}{2}, \frac{l}{4}\right)$, an indication of a four-layer lattice periodicity along the out-of-plane direction, which is consistent with the quadruple lattice of $Pbcm$ in the presence of complicated rotation patterns $a^+b^-c^-/a^-b^-c^-$, $a^-b^+c^-/a^-b^-c^-$, and $a^-b^-c^+/a^-b^-c^-$ (Figure 3e). Therefore, the half-order XRD peaks were further used to probe the structural characteristics that pertain to the $Pmc2_1$ and $Pbcm$ space groups, respectively.

2.3.3. Second-Harmonic Generation Measurements

The coexistence of ferroelectric and antiferroelectric phases also results in a dramatic spatial variation of the non-linear optical response, which can be probed by SHG measurements with a transverse-polarized fundamental beam in a normal incidence geometry to probe the in-plane symmetry breaking. A SHG map measured on a 160 nm-thick $NaNbO_3$ membrane shows an intensity variation arising from the coexistence of phases with distinct symmetry, in which the bright intensity is produced by the non-centrosymmetric ferroelectric phase whereas the dark intensity is generated by the centrosymmetric antiferroelectric phase (see Experimental Section and Figure 3d). Furthermore, to elucidate the point group symmetry of the ferroelectric phase, polar plots were measured from the ferroelectric phase as a function of incident beam polarization (Figure 3g,h). The emitted vertically (Figure 3g) and horizontally (Figure 3h) polarized SHG signals can be fitted using the symmetry-based SHG tensor, for which we obtain fitting results consistent with the orthorhombic $mm2$ point group symmetry (see Experimental Section).[35] Since the space group $Pmc2_1$ is a subclass of $mm2$, the SHG measurements further verified the orthorhombic structural nature of the ferroelectric phase in $NaNbO_3$ membranes.

2.4. Nanomechanical Measurements Showing a Non-Monotonic Thickness Dependence of Young's Modulus

We also studied how this size-dependent structural evolution impacts the elastic properties of the $NaNbO_3$ membranes. We probed the elastic response using an atomic force microscopy (AFM)-based method, in which an AFM tip was

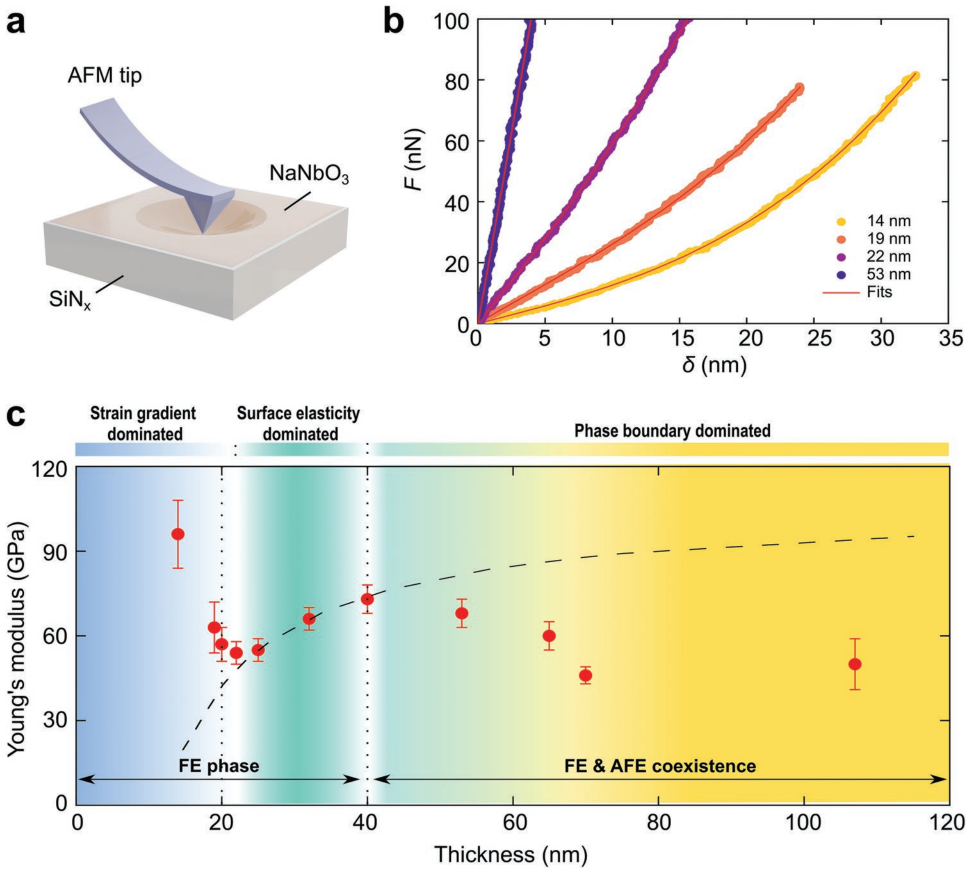

Figure 4. AFM-based nanomechanical measurements on NaNbO$_3$ membranes as a function of thickness. a) Schematic diagrams illustrating the drumhead deformation upon local bending by an AFM tip. b) Representative force–deflection curves showing the linear response for $t > 25$ nm and the presence of both the linear and non-linear response for $t < 25$ nm. c) Young's modulus extracted from the linear response showing a highly non-monotonic thickness dependence, which is governed by strain gradient and surface elasticity in the single-phase regime below 40 nm and dominated by contributions from the phase boundaries in the mixed-phase regime. The dashed line shows the trend of approaching the Young's modulus of bulk NaNbO$_3$ above 120 nm. The error bars were generated by including an estimated 10% uncertainty in the spring constant calibration and the standard error of the mean.

utilized to measure the force (F)–displacement (δ) response by deflecting the freestanding oxide drumhead formed over the holes of the SiN$_x$ membrane (**Figure** 4a). For $t > 25$ nm, a linear F–δ response was observed, whereas for $t < 25$ nm, an additional non-linear F–δ response was seen at higher deflection (Figure 4b). The linear and non-linear responses can be attributed to a bending and stretching dominated deformation of the membrane, respectively. By analyzing these two deformation regimes, the Young's modulus including the bending stiffness E_{lin} and stretching stiffness E_{cub} can be extracted from the linear and the non-linear response, respectively, as a function of film thickness (see Experimental Section and Figures S18 and S19, Supporting Information). A highly non-monotonic thickness dependence of E_{lin} was observed in the NaNbO$_3$ membranes (Figure 4c). For $t < 20$ nm, the measured Young's modulus increases sharply to 100 GPa with reducing thickness, whereas for 20 nm $< t <$ 40 nm, E_{lin} shows an opposite trend which decreases with reducing thickness. Such a thickness dependence of Young's modulus resembles the trend observed in SrTiO$_3$ membranes,[36] in which a strain gradient elastic contribution causes an upturn in E_{lin} for $t < 20$ nm (i.e., $\Delta E_{\mathrm{lin}} \propto 1/t^2$), while a surface elasticity contribution results in a decrease in E_{lin} with reducing thickness for 20 nm $< t <$ 40 nm (i.e., $\Delta E_{\mathrm{lin}} \propto -1/t$). Therefore, up to 40 nm thickness, the trend can be well understood using a single-phase model.

Following such a single-phase model, E_{lin} should ultimately approach the bulk Young's modulus of NaNbO$_3$ (dashed line, Figure 4c). Instead of increasing further toward the bulk value, however, E_{lin} starts decreasing at $t > 40$ nm. This thickness regime coincides with the emergence of a mixture of ferroelectric and antiferroelectric phase in NaNbO$_3$ membranes. Such a reduced Young's modulus is likely due to the presence of geometrical phase boundaries in the mixed phase state, which allow for greater deformation upon loading, and thus leading to a lower Young's modulus. Similar phenomena have been demonstrated in polycrystalline materials where the atoms at the grain boundaries show higher compliance due to their higher mobility, and thereby giving rise to a lower overall Young's modulus.[37–41] Similarly, our result wherein E_{lin} decreases with thickness is also a possible result of increasing contributions from the phase boundaries as the volume fraction of the *Pbcm* phase increases with thickness. In addition, since the AFM-based method only allows for the measurement up to ≈100 nm (i.e., the compliance of membranes at t > 100 nm approaches the value of SiN_x membrane which makes the analysis difficult), we also performed nanoindentation tests to verify the trend beyond this thickness range (see Experimental Section and Figure S20 and Note S2, Supporting Information). Overall, these results indicate that the non-monotonic thickness dependence of Young's modulus is coupled to the emergent phase transition in $NaNbO_3$ membranes, which is governed by the strain gradient and surface elasticity in the single-phase regime, and dominated by contributions from the phase boundaries in the mixed-phase regime.

In addition, we also obtained the value of pre-strain from the nanomechanical analysis performed in the linear response regime of the suspended membranes.[36] Figure S21, Supporting Information, shows a very small amount of pre-strain (<0.1%) for all $NaNbO_3$ membranes, regardless of thickness. These results again indicate that the effects of strain are negligible on the lifted-off membranes.

2.5. First-Principle Calculations Unveiling the Transition Mechanism

So, what drives this emergent antiferroelectric-to-ferroelectric transition in $NaNbO_3$ membranes? First-principle calculations based on density functional theory (DFT) were performed to understand the mechanism. Since apparently the surface contribution increases with reducing film thickness, we considered the surface effects by calculating symmetric $NaNbO_3$ (001) slabs with defective NaO surfaces as a function of thickness (see Experimental Section). For the largest studied thickness of 9 formula units (f.u.), we found that the antiferroelectric-like phase is more stable, with an energy difference $\Delta E = -16.62$ meV (with $\Delta E = E_{\mathrm{Pbcm}} - E_{\mathrm{Pmc2_1}}$), consistent with the case for the unstrained bulk $NaNbO_3$ (Note S2, Supporting Information). By reducing the thickness to 7 f.u., ΔE increases such that the $Pmc2_1$ phase becomes more stable over the *Pbcm* phase, with $\Delta E = +6.96$ meV (**Figure 5**). Such a thickness-dependent structural evolution is qualitatively consistent with the experimental observations. Note that the calculated c/a ratio (0.995) for the $Pmc2_1$ phase is very close to the experimental results ($(c/a)_{\mathrm{exp}} = 0.993–0.997$) measured for a membrane thickness from 20 to 40 nm (Figure S4, Supporting Information). In addition, it was noted from the experiment that the c/a ratio for the *Pbcm* phase is lower than the $Pmc2_1$ phase, which are 0.986 and 0.998 respectively, measured for 65 nm-thick membranes (Figure S4, Supporting Information). Given our numerical results showing that the c/a ratio increases with reduced film thickness, it is possible that the higher tetragonality, resulting from the structural relaxation induced by the surface, helps stabilize the $Pmc2_1$ phase, whereas when the thickness increases, some volume fraction of the membrane relaxes to a lower c/a ratio, which induces the emergence of the *Pbcm* phase. Therefore, the DFT calculations reveal that the experimentally observed emergence of the $Pmc2_1$ phase is a possible result of the structural distortions induced by the surface. Note, however, that many factors were not taken into account in the calculations, which may explain that the agreement between experiments and theory is qualitative rather than quantitative (the predicted critical thickness from a $Pmc2_1$ to a *Pbcm* phase is ≈2.7 nm, which is lower than the experimentally observed critical thickness of 40 nm). Examples of such factors are the presence of structural defects, inhomogeneities, surfaces having other reconstructions and terminations, and thickness commensurability/incommensurability with the *Pbcm*-phase period (Note S3, Supporting Information).

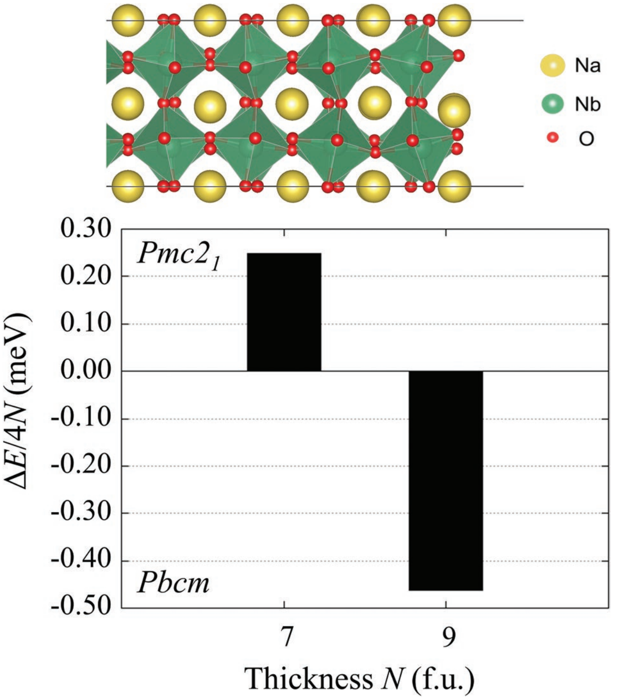

Figure 5. First-principle calculations on $NaNbO_3$ membranes. Energy difference ($\Delta E = E_{Pbcm} - E_{Pmc21}$) calculated between the antiferroelectric *Pbcm* and ferroelectric $Pmc2_1$ phases for a 2 × 2 × N slab with a Na_4O_3 terminated surface. The slab energy differences ΔE were normalized and are not directly comparable with bulk values because the slabs are not stoichiometric.

In addition, we cannot neglect the possibility that the ferroelectricity measured in $NaNbO_3$ membranes is a result of the frozen ferroelectricity in their initial as-grown state. Note that the *Pbcm* antiferroelectric phase is more stable than the ferroelectric $Pmc2_1$ phase when $NaNbO_3$ is unstrained. Therefore, the ferroelectric phase is favored in the as-grown $NaNbO_3$ on $SrTiO_3$. The relaxation from the strained ferroelectric phase to the unstrained antiferroelectric phase would require overcoming an energy barrier ≈33 meV f.u.$^{-1}$, calculated using the nudged elastic band method,[42,43] which is two orders of magnitude higher than the energy difference between the two phases at equilibrium. If such an energy barrier increases in thin membranes due to dimensionality or surface effects, the thin membranes could remain frozen in their initial ferroelectric state during the lift-off process.

3. Conclusions

Our work demonstrates the intrinsic scaling of $NaNbO_3$ membranes driven by the structural distortion arising from the surface, leading to an intriguing antiferroelectric-to-ferroelectric transition with reducing thickness. Specifically, we probe a single ferroelectric phase state below 40 nm and a mixed-phase state above this critical thickness with the coexistence of ferroelectric and antiferroelectric orders. The observed coexisting ferroelectric and antiferroelectric phases are also electrically switchable. Detailed optical characterizations further reveal the structural nature of these two phases, which are $Pmc2_1$ and $Pbcm$ space group symmetries for the ferroelectric and antiferroelectric phase, respectively. Our work demonstrates enormous potential of utilizing size effects to drive emergent properties in environmentally benign oxide materials with the membrane platform.

4. Experimental Section

Thin-Film Growth: The epitaxial heterostructures of 9–164 nm-thick $NaNbO_3$ and 20 nm-thick $La_{0.7}Sr_{0.3}MnO_3$ were synthesized on (001)-oriented single-crystalline $SrTiO_3$ substrates via PLD. The $La_{0.7}Sr_{0.3}MnO_3$ sacrificial layer was grown first at a growth temperature of 700 °C, an oxygen pressure of $1.9–2.1 \times 10^{-1}$ Torr, an imaged laser spot size of 5.86 mm^2, a laser fluence of 1.50 J cm^{-2}, and a repetition rate of 3 Hz. The $NaNbO_3$ layer was then synthesized in the same chamber at a growth temperature of 600 °C, an oxygen pressure of $2.0–2.4 \times 10^{-1}$ Torr, an imaged laser spot size of 5.86 mm^2, a laser fluence of 1.60 J cm^{-2}, and a repetition rate of 2 Hz. Following growth, the chamber was cooled down to room temperature in 1.5 torr O_2 at a cooling rate of 5 °C min^{-1}.

Piezoresponse Force Microscopy: The PFM measurements were taken with a Cypher AFM (Asylum Research) using Ir/Pt-coated conductive tips with a force constant of ≈2.8 N m^{-1} (Nanosensor, PPP-EFM). Vector PFM mode was used to allow for simultaneous measurement of both the in-plane and out-of-plane polarization domain structure.

$NaNbO_3$ Membrane Transfer: A 600 nm-thick poly(methyl methacrylate) (PMMA) support layer was first spin coated on top of the heterostructure and baked at 135 °C. The heterostructure was then placed in a solution of 5 g KI + 0.5 mL 6 м HCl + 50 mL deionized water at room temperature for 4–6 days until the $La_{0.7}Sr_{0.3}MnO_3$ had been fully dissolved. The PMMA-coated $NaNbO_3$ film was then released from the $SrTiO_3$ substrate and transferred onto 200 nm-thick perforated SiN_x membranes with circular holes in diameter of 2, 5, or 10 µm, supported by 200 µm Si frame (Norcada Inc.). The PMMA support layer was then removed by dissolving in acetone at 60 °C and then washing in isopropanol, leaving just the freestanding $NaNbO_3$ membrane.

Raman Spectroscopy: The Raman spectroscopy measurements were conducted using a Horiba LabRAM HR Evolution spectrometer with a 100× SWD objective. A HeNe gas laser was used to produce a linear polarized incident light with a wavelength of 633 nm, an average power of 8 mW, and a spot size of 448 nm. The Raman spectra were measured on the suspended $NaNbO_3$ drumheads on SiN_x membranes in a range of 30–1000 cm^{-1} with an ultralow frequency filter at a cut-off of ≈5 cm^{-1}. The 2D Raman mapping was measured in a spectral window of 85–410 cm^{-1} on a 164 nm-thick $NaNbO_3$ membrane transferred onto an Al_2O_3 substrate, which had a minimal Raman signal for the peaks of interest around 180 cm^{-1}.

Second-Harmonic Generation: SHG measurements were carried out in a normal-incidence, reflection-geometry. A Ti/sapphire oscillator was used for light excitation with ≈100 fs pulses and center wavelength of 900 nm, a 78 MHz repetition rate, and an average power of <1 mW. To arbitrarily control the polarization of the incoming light, a Glan–Thompson polarizer was used and subsequently the light was sent through a half-waveplate. The polarized light was then sent through a short-pass dichroic mirror and focused on the sample using a 100× (NA = 0.95) objective. The back-scattered SHG signal was sent through a short-pass filter and detected using a spectrometer (SpectraPro 500i, Acton Research Instruments) with a charge-coupled device camera (Andor iXon CCD). A linear polarizer on the back-end optics was used to select emitted light polarization for detection. Diffraction-limited confocal scanning microscopy was used to create SHG intensity maps. A commercial Thorlabs polarimeter was used at the sample location to confirm the incoming light polarization incident on the sample, as well as the light polarization entering the detector. All SHG maps shown throughout the manuscript were performed using $[100]_{pc}$-polarized incident light with no polarizer on the back-end optics.

The analysis of SHG polar plots was conducted using a non-linear tensor for the orthorhombic system. First, the non-linear polarization of each domain variant could be described using an $mm2$ point group tensor:

$$\begin{pmatrix} P_1 \\ P_2 \\ P_3 \end{pmatrix} = \begin{pmatrix} 0 & 0 & 0 & 0 & d_{15} & 0 \\ 0 & 0 & 0 & d_{24} & 0 & 0 \\ d_{31} & d_{32} & d_{33} & 0 & 0 & 0 \end{pmatrix} \begin{pmatrix} E_1^2 \\ E_2^2 \\ E_3^2 \\ 2E_2E_3 \\ 2E_1E_3 \\ 2E_1E_2 \end{pmatrix} \tag{1}$$

where P_i (i = 1, 2, 3) and E_i (i = 1, 2, 3) were defined in the local coordinate system for each domain variant (X_1, X_2, X_3) with X_1 parallel to the polarization direction in each domain. In order to analyze the polar plots which were measured with respect to the reference frame of (x_1, x_2, x_3), wherein x_1, x_2, x_3 were parallel to the pseudocubic crystal axes [100], [010], and [001], the non-linear response needed to be converted from the local coordinate system (X_1, X_2, X_3) to the global coordinate system (x_1, x_2, x_3).

For example, for the domain variant 2, the electric field (E_1, E_2, E_3) in the local coordinate system could be converted into (E_x, E_y, E_z) in the global coordinate system, using the following transformation matrix:

$$\begin{bmatrix} -\frac{\sqrt{2}}{2} & 0 & -\frac{\sqrt{2}}{2} \\ 0 & 1 & 0 \\ \frac{\sqrt{2}}{2} & 0 & -\frac{\sqrt{2}}{2} \end{bmatrix} \tag{2}$$

Therefore, the following relation could be obtained:

$$E_1 = -\frac{\sqrt{2}}{2}(E_x + E_z),\ E_2 = E_y,\ E_3 = \frac{\sqrt{2}}{2}(E_x - E_z) \tag{3}$$

Since the normal incidence beam produced electrical components $E^{\omega}(\varphi) = (E_0 sin\varphi,\ E_0 cos\varphi,\ 0)$, where φ was the azimuthal angle of the fundamental light polarization, the electric field components could be further written as:

$$E_1 = -\frac{\sqrt{2}}{2}E_0 \sin\varphi,\ E_2 = E_0 \cos\varphi,\ E_3 = \frac{\sqrt{2}}{2}E_0 \sin\varphi \tag{4}$$

Using Equation (1), the following relation for the non-linear polarization in the domain variant 2 was derived,

$$\begin{aligned} &P_1 = -E_0^2 d_{15} \sin^2\varphi, \\ &P_2 = E_0^2 \frac{d_{24}}{\sqrt{2}} \sin 2\varphi, \\ &P_3 = E_0^2 \left(\frac{d_{31} + d_{33}}{2} \sin^2\varphi + d_{32} \cos^2\varphi \right) \end{aligned} \tag{5}$$

Transforming Equation (5) back to the reference frame of (x_1, x_2, x_3), the following was obtained:

$$P_x = -\frac{1}{\sqrt{2}}\left(E_0^2\left(\frac{d_{31}+d_{33}}{2}\sin^2\varphi + d_{32}\cos^2\varphi\right) + E_0^2 d_{15}\sin^2\varphi \right) \tag{6}$$

$$P_y = E_0^2\frac{d_{24}}{\sqrt{2}}\sin 2\varphi \tag{7}$$

$$P_z = -\frac{1}{\sqrt{2}}\left(E_0^2\left(\frac{d_{31}+d_{33}}{2}\sin^2\varphi + d_{32}\cos^2\varphi\right) - E_0^2 d_{15}\sin^2\varphi \right) \tag{8}$$

Similar conversions could also be carried out for other domain variants. Taking account of the contributions from all possible domain variants, the angular dependence of the total SHG intensity was found as

$$\begin{aligned} I_j^{2\omega} &= K_{1,j}\left(\cos^2\varphi + K_{2,j}\sin^2\varphi\right)^2 + K_{3,j}\sin^2 2\varphi \\ &\quad + K_{4,j}\left(\cos^2\varphi + K_{2,j}\sin^2\varphi\right)\sin 2\varphi \end{aligned} \tag{9}$$

which could well fit the experimental polar plots.

X-Ray Diffraction: XRD symmetric θ–2θ line scans were performed using a Bruker D8 Discover with a monochromated Cu $K_{\alpha 1}$ (λ = 1.5406 Å) source. Synchrotron XRD measurements including 3D RSM and detailed half-order super-reflections were carried out on a five-circle Huber diffractometer with Chi geometry using an X-ray energy of 20 keV (wavelength $\lambda = 0.6199$ Å) at the beamline sector 12-ID-D in the Advanced Photon Source (APS) at the Argonne National Laboratory. A Si (111) double crystal monochromator with a resolution $\Delta E/E = 1\times10^{-4}$ was used to manipulate and set X-ray energy. The X-ray beam had a total flux of 2×10^{12} photons/s at 20 KeV, and the beam was vertically de-magnified by a 1D focusing compound refractive lenses. An X-ray beam profile of 50 µm (V) × 500 µm (H) was used in the measurement. The scattering signals were captured by a Pilatus 100K 2D area detector, and the 2D images were used to perform the data processing. Geometric corrections were applied for all 3D RSM and half-order super-reflection data. RSM data were processed by the RSMap3D software developed by APS.

Nanomechanical Measurements via Atomic Force Microscopy: The AFM measurements were taken with a Cypher AFM (Asylum Research) using BudgetSensors Multi75DLC carbon-coated tips, which had a force constant of ≈3 N m^{-1}, a tip radius of ≈15 nm, and a free-space resonance frequency of ≈75 kHz. $NaNbO_3$ thicknesses were determined by averaging step heights at several locations at the edge of the freestanding membranes. To acquire the force–deflection curves, the AFM tip contacted the $NaNbO_3$ membranes at 32 × 32 positions across an entire freely suspended drumhead as well as some of the surrounding region supported by SiN_x. A maximum force of ≈100 nN was applied to the freestanding membranes. For the thinner membranes, this caused both a linear (bending dominated) and non-linear (stretching dominated) force–deflection response whereas only a linear response could be measured in the thicker membranes. To extract Young's modulus from the linear response force–deflection curves (E_{lin}), a fit to the experimental compliance map was performed. Compliance was calculated by extracting the slope of the linear force–deflection at each of the 32 × 32 positions of the force map. The fit was performed by numerically solving the bending equation with clamped boundary conditions using the finite element solver FeNICS.

$$\frac{E_{\text{lin}}t^3}{\left[12\left(1-\upsilon^2\right)\right]}\nabla^4 u(r) - T\nabla^2 u(r) = p(r) \tag{10}$$

where t is the membrane thickness, ν is the Poisson ratio (0.25 typical for perovskite oxides), T is the uniform pretension of the membrane, and E_{lin} is the Young's modulus extracted from the bending response. These could be used to fully describe mechanical deformation $u(r)$ under a loading pressure $p(r)$ with the general biharmonic equation (with r describing the in-plane position).

For the non-linear force–deflection response Young's modulus (which was dominated by a stretching response), only the curve at the center of the drumhead was used and the response was fit to a cubic polynomial of the form

$$F = A\delta + B\delta^3 \tag{11}$$

where δ is the deflection of the membrane from its neutral position and the coefficient B is proportional to the Young's modulus (E_{cub}) to be inferred from the non-linear response. Further details on both the measurement and analysis were described previously in the work by Harbola et al. and were adapted for this measurement.

Nanoindentation Tests: Nanoindentation tests were performed using the iMicro nanoindenter (Nanomechanics, Inc.) and a diamond Berkovich tip (Synton-MDP) to obtain the elastic modulus of the thin film. Samples with a top layer of 160 nm-thick $NaNbO_3$ membrane, an intermediate layer of 300 nm-thick SiO_2, and a Si substrate layer were indented with a continuous stiffness measurement method to a target depth of 100 nm, strain rate of 0.2 s^{-1}, target frequency of 110 s^{-1}, and target dynamic displacement (amplitude of oscillation) of 2 nm to measure elastic modulus as a function of depth.

First-Principle Calculations: First-principle calculations based on the DFT were performed by employing the projector augmented-wave method,[44] as implemented in the Vienna Ab initio Simulation Package code[45] and using the generalized gradient approximation, within the Perdew–Burke–Ernzerhof functional for solids.[46] A plane-wave basis set with a kinetic energy cut-off of 550 eV was used. The valence states used for the calculations were $2p^63s^1$ for Na, $4s^24p^64d^45s^1$ for Nb, and $2s^22p^4$ for O, respectively.

Slabs were built symmetrically, with two identical (001) surfaces, starting from the *Pbcm* or *Pmc*2$_1$ optimized bulk structure. The slab resulting space groups might be different due to the reduced symmetries imposed by the presence of the surfaces, but it was verified that the same ferroelectric or antiferroelectric ordering as in the bulk was preserved. The slab thicknesses were ≈2.7 or 3.5 nm, which corresponded to 7–9 f.u. of $NaNbO_3$ plus an additional atomic layer. A vacuum thickness of more than 20 Å was added to avoid spurious interactions between the two surfaces. Considering that the films were free-standing and quite thin, a structural optimization was performed to release the in-plane strain and to calculate optimum in-plane and out-of-plane lattice parameters. Optimized structures were obtained with Hellmann–Feynman forces on each atom converged to less than 0.005 eV Å^{-1}. Perfect (001) surfaces could either have a NaO or a NbO_2 termination. The discussion was focused on the NaO surfaces as it was found that they displayed calculated average c/a ≈0.995 ratios which show the best match with the measurements. Results obtained with the other surface terminations are described in Note S3 and Figure S22, Supporting Information. Because (001) NaO and NbO_2 atomic layers were charged, (2 × 2) NaO surfaces were studied including an oxygen vacancy to preserve the insulating behavior of the film. The new surface termination was thus made of Na_4O_3, but for the sake of simplicity it was decided to simply continue to name it NaO.

Supporting Information

Supporting Information is available from the Wiley Online Library or from the author.

Acknowledgements

R.X., K.J.C., and V.H. contributed equally to this work. The authors acknowledge assistance in the Raman measurement from Dr. Jennifer Fowlie. This work was supported by the Division of Materials Sciences and Engineering, Office of Basic Energy Sciences (DOE-BES), U.S. Department of Energy, under contract no. DE-AC02-76SF00515. This work was granted access to the HPC resources of CALMIP (Allocation No. 2022/P19004). This research used resources of the Advanced Photon Source, a U.S. Department of Energy (DOE) Office of Science user facility operated for the DOE Office of Science by Argonne National Laboratory under Contract No. DE-AC02-06CH11357. Second-harmonic generation at the Molecular Foundry was supported by the Office of Science, Office of Basic Energy Sciences, of the U.S. Department of Energy under Contract No. DE-AC02-05CH11231. Raman spectroscopy was performed at the Stanford Nano Shared Facilities (SNSF), supported by the National Science Foundation under award ECCS-1542152. K.Y.P., S.P., L.B., P.B., L.W.M., and R.R. acknowledge support of the Army Research Office under the MURI ETHOS via cooperative agreement W911NF-21-2-0162. K.Y.P. and L.B. are thankful for the support from the Vannevar Bush Faculty Fellowship (VBFF) Grant No. N00014-20-1-2834 from the Department of Defense. S.P. and L.B. also acknowledges the support from the Office of Naval Research Grant No. N00014-21-1-2086. H.Y.H., Y.-T.S., D.A.M., and R.R. acknowledges support of Air Force Office of Scientific Research (AFOSR) Hybrid Materials MURI under award no. FA9550-18-1-0480. M.A. acknowledges support from the Materials Sciences and Engineering Division, Office of Basic Energy Sciences, Office of Science, U.S. Department of Energy, under Contract No. DE-AC02-05-CH11231 (Materials Project program KC23MP) for the development of novel antiferroelectric materials. L.W.M. acknowledges additional support from the Army Research Office under grant W911NF-21-1-0118. R.X. acknowledges partial support by the start-up funding from North Carolina State University . L.C. acknowledges financial support from the Ford Foundation and the University of California President's Postdoctoral Fellowship Program. M.M.W. is supported by the National Science Foundation Graduate Research Fellowship under Grant DGE-1656518. X.W.G. and M.M.W. acknowledge support from the U.S. Department of Energy, under contract No. DE-SC0021075.

Conflict of Interest

The authors declare no conflict of interest.

Data Availability Statement

The data that support the findings of this study are available from the corresponding author upon reasonable request.

Keywords

antiferroelectric materials, membranes, phase transition, size effects, sodium niobate

Received: November 14, 2022
Revised: January 6, 2023

---

[1] J. F. Ihlefeld, D. T. Harris, R. Keech, J. L. Jones, J. P. Maria, S. Trolier-McKinstry, *J. Am. Ceram. Soc.* **2016**, *99*, 2537.
[2] P. Ghosez, K. M. Rabe, *Appl. Phys. Lett.* **2006**, *76*, 2767.
[3] S. S. Cheema, D. Kwon, N. Shanker, R. dos Reis, S. Hsu, J. Xiao, H. Zhang, R. Wagner, A. Datar, M. R. Mccarter, C. R. Serrao, A. K. Yadav, G. Karbasian, C. Hsu, A. J. Tan, L. Wang, V. Thakare, X. Zhang, A. Mehta, *Nature* **2020**, *580*, 478.
[4] R. Xu, R. Gao, S. E. Reyes-lillo, S. Saremi, Y. Dong, H. Lu, Z. Chen, X. Lu, Y. Qi, S. Hsu, A. R. Damodaran, H. Zhou, B. Neaton, L. W. Martin, *ACS Nano* **2018**, *12*, 4736.
[5] S. Li, J. A. Eastman, J. M. Vetrone, C. M. Foster, R. E. Newnham, L. E. Cross, *Jpn. J. Appl. Phys.* **1997**, *35*, 5169.
[6] E. A. Eliseev, S. V. Kalinin, A. N. Morozovska, *J. Appl. Phys.* **2015**, *117*, 034102.
[7] J. Junquera, P. Ghosez, *Nature* **2003**, *422*, 506.
[8] M. Dawber, P. Chandra, P. B. Littlewood, J. F. Scott, *J Phys Condens Matter* **2003**, *15*, L393.
[9] Y. J. Shin, Y. Kim, S. J. Kang, H. H. Nahm, P. Murugavel, J. R. Kim, M. R. Cho, L. Wang, S. M. Yang, J. G. Yoon, J. S. Chung, M. Kim, H. Zhou, S. H. Chang, T. W. Noh, *Adv. Mater.* **2017**, *29*, 1602795.
[10] R. J. Ong, D. A. Payne, N. R. Sottos, *J. Am. Ceram. Soc.* **2005**, *2847*, 2839.
[11] D. Ji, S. Cai, T. R. Paudel, H. Sun, C. Zhang, L. Han, Y. Wei, Y. Zang, M. Gu, Y. Zhang, W. Gao, H. Huyan, W. Guo, D. Wu, Z. Gu, E. Y. Tsymbal, P. Wang, Y. Nie, X. Pan, *Nature* **2019**, *570*, 87.
[12] C. A. Randall, Z. Fan, I. Reaney, L. Q. Chen, S. Trolier-McKinstry, *J. Am. Ceram. Soc.* **2021**, *104*, 3775.
[13] Z. Liu, T. Lu, J. Ye, G. Wang, X. Dong, R. Withers, *Adv. Mater. Technol.* **2018**, *3*, 1800111.
[14] B. K. Mani, C. M. Chang, S. Lisenkov, I. Ponomareva, *Phys. Rev. Lett.* **2015**, *115*, 097601.
[15] D. Lu, D. J. Baek, S. S. Hong, L. F. Kourkoutis, Y. Hikita, H. Y. Hwang, *Nat. Mater.* **2016**, *15*, 1255.
[16] S. S. Hong, M. Q. Gu, M. Verma, V. Harbola, B. Y. Wang, D. Lu, A. Vailionis, Y. Hikita, R. Pentcheva, J. M. Rondinelli, H. Y. Hwang, *Science* **2020**, *368*, 71.
[17] D. Lu, S. Crossley, R. Xu, Y. Hikita, H. Y. Hwang, *Nano Lett.* **2019**, *19*, 3999.
[18] R. Xu, J. Huang, E. S. Barnard, S. S. Hong, P. Singh, E. K. Wong, T. Jansen, V. Harbola, J. Xiao, B. Y. Wang, S. Crossley, D. Lu, S. Liu, H. Y. Hwang, *Nat. Commun.* **2020**, *11*, 3141.
[19] S. R. Bakaul, C. R. Serrao, M. Lee, C. W. Yeung, A. Sarker, S. L. Hsu, A. K. Yadav, L. Dedon, L. You, A. I. Khan, J. D. Clarkson, C. Hu, R. Ramesh, S. Salahuddin, *Nat. Commun.* **2016**, *7*, 10547.
[20] D. Pesquera, E. Parsonnet, A. Qualls, R. Xu, A. J. Gubser, J. Kim, Y. Jiang, G. Velarde, Y. Huang, H. Y. Hwang, R. Ramesh, L. W. Martin, *Adv. Mater.* **2020**, *32*, 2003780.
[21] Y. Yang, B. Xu, C. Xu, W. Ren, L. Bellaiche, *Phys. Rev. B* **2018**, *97*, 174106.
[22] K. Patel, S. Prosandeev, B. Xu, C. Xu, L. Bellaiche, *Phys. Rev. B* **2021**, *094103*, 094103.
[23] S. K. Mishra, N. Choudhury, S. L. Chaplot, P. S. R. Krishna, R. Mittal, P. Nanbo, *Phys. Rev. B* **2007**, *76*, 024110.
[24] K. E. Johnston, C. C. Tang, J. E. Parker, K. S. Knight, P. Lightfoot, S. E. Ashbrook, *J. Am. Chem. Soc.* **2010**, *132*, 8732.
[25] J. Schwarzkopf, D. Braun, M. Hanke, R. Uecker, M. Schmidbauer, *Front. Mater.* **2017**, *4*, 26.
[26] R. H. Dungan, R. D. Golding, *J. Am. Ceram. Soc.* **1964**, *47*, 73.
[27] Y. Shiratori, A. Magrez, J. Dornseiffer, F. H. Haegel, C. Pithan, R. Waser, *J. Phys. Chem. B* **2005**, *109*, 20122.
[28] S. Chattopadhyay, P. Ayyub, V. R. Palkar, A. V. Gurjar, *J Phys Condens Matter* **1997**, *9*, 8135.
[29] A. Duk, M. Schmidbauer, J. Schwarzkopf, *Appl. Phys. Lett.* **2013**, *102*, 2011.
[30] J. Schwarzkopf, D. Braun, M. Schmidbauer, A. Duk, R. Wördenweber, *J. Appl. Phys.* **2014**, *115*, 204105.
[31] Z. X. Shen, X. B. Wang, M. H. Kuok, S. H. Tang, *J. Raman Spectrosc.* **1998**, *29*, 379.
[32] K. K. Mishra, V. Sivasubramanian, A. K. Arora, *J. Raman Spectrosc.* **2011**, *42*, 517.
[33] M. Jauhari, S. K. Mishra, R. Mittal, S. L. Chaplot, *J. Raman Spectrosc.* **2019**, *50*, 1177.
[34] A. M. Glazer, *Acta Crystallogr., Sect. A: Found. Crystallogr.* **1975**, *31*, 756.
[35] V. Gopalan, R. Raj, *J. Appl. Phys.* **1997**, *81*, 865.
[36] V. Harbola, S. Crossley, S. S. Hong, D. Lu, Y. A. Birkhölzer, Y. Hikita, H. Y. Hwang, *Nano Lett.* **2021**, *21*, 2470.
[37] J. Schiøtz, F. D. Di Tolla, K. W. Jacobsen, *Nature* **1998**, *391*, 561.

[38] R. Chaim, M. Hefetz, *J. Mater. Sci.* **2004**, *39*, 3057.
[39] T. Y. Kim, J. E. Dolbow, E. Fried, *Int. J. Solids Struct.* **2012**, *49*, 3942.
[40] M. Becton, X. Wang, *Phys. Chem. Chem. Phys.* **2015**, *17*, 21894.
[41] L. Zhu, X. Zheng, *Acta Mech.* **2010**, *213*, 223.
[42] G. Henkelman, H. Jónsson, *J. Chem. Phys.* **2000**, *113*, 9978.
[43] G. Henkelman, B. P. Uberuaga, H. Jónsson, *J. Chem. Phys.* **2000**, *113*, 9901.
[44] P. E. Blöchl, *Phys. Rev. A* **1994**, *50*, 17953.
[45] G. Kresse, J. Furthmuller, *Phys. Rev. B* **1996**, *54*, 11169.
[46] J. P. Perdew, A. Ruzsinszky, I. Csonka, O. A. Vydrov, G. E. Scuseria, L. A. Constantin, J. P. Perdew, A. Ruzsinszky, X. Zhou, K. Burke, *Phys. Rev. Lett.* **2008**, *100*, 136406.